




Reconstruction for beam blockage of lidar based on generative adversarial networks

HAOYU YANG,¹ JINLONG YUAN,^{1,3} LI GUAN,¹ LIAN SU,² TIANWEN WEI,¹ AND HAIYUN XIA^{1,2,4} 

¹*School of Atmospheric Physics, Nanjing University of Information Science and Technology, Nanjing 210044, China*

²*School of Earth and Space Science, University of Science and Technology of China, Hefei 230026, China*

³*yuanjinlong@nuist.edu.cn*

⁴*hsia@ustc.edu.cn*

Abstract: Doppler lidar is an active laser remote sensing instrument. However, beam blockage caused by low-altitude obstacles is a critical factor affecting the quality of lidar data. To reconstruct the line of sight velocities (LOS_V) in areas with beam blockages and to evaluate the effectiveness of reconstruction results, the LOS_V-filling network (LFnet) approach based on generative adversarial networks (GANs) and an evaluation scheme based on the degree of blockage are proposed in this paper. The LFnet comprises two adversarial models. The first adversarial model captures the structural features of LOS_V to output the edge map, and the second adversarial fills in the blockage area using the edge map. We have built a packaged dataset consisting of training, validation and test datasets with mask sets. Then the sensitivity of the reconstruction effectiveness with different shielding conditions is studied, to reveal the mechanism of shielding influencing the reconstruction. A series of indicators were used to evaluate the model's performance, including the traditional indicators and the proposed indicator of root mean square error (RMSE). Finally, LFnet was demonstrated in a practical application in an airport. The complete process of an easterly gust front is reconstructed with RMSE less than 0.85 m/s, which has significance for flight safety.

© 2024 Optica Publishing Group under the terms of the [Optica Open Access Publishing Agreement](#)

1. Introduction

Coherent Doppler wind lidar (CDWL) is a remote sensing instrument with the advantages of compact size and a high temporal-spatial resolution. It has been widely used in atmospheric wind field detection [1,2], including atmospheric turbulence [3,4], wind gusts [5], wind shear [6–10] and aircraft vortices [11]. However, the laser propagation is blocked by low-altitude buildings, terrain, or other obstacles, resulting in a phenomenon known as beam blockage. The lidar echo signals in these azimuths may be weakened or eliminated, affecting the product's quality. For example, lack of key line of sight velocities (LOS_V) may lead to imprecise wind shear identification [6]. Reconstruction of beam blockage is crucial to improve the quality of CDWL detection data.

Research on beam blockage reconstruction primarily focuses on the application of weather radars, with the method of high-resolution Digital Elevation Models (DEM) [12,13], spatial correlation based methods [14] and deep learning-based methods [15]. The DEM is a digital data model that describes the elevation information of the earth's surface and calculates the power loss in the received signal based on the geometrical relationship between radar beams and a DEM. A new method for the mitigation of partial beam blockage, which uses the consistency between the reflectivity factor Z and specific differential phase K_{DP} and their radial integrals in the rain, is presented by Zhang et al. [13]. However, trees, buildings and other objects not accounted for in the DEM may cause additional blockage. The radar signal processing utilizes a spatial correlation-based identification algorithm to detect and identify obstacles encountered

by radar beams during their propagation [14]. The algorithm's fundamental premise is to distinguish obstacle interference from signal noise by employing the spatial correlation of the beams. It is dependent on adjacent radial echo and adjacent high-elevation echo data. Based on Convolutional Neural Networks (CNNs), the reflectance factor Z_H and differential reflectance Z_{DR} of the unobstructed area are employed to fill Z_H and Z_{DR} of the obstructed areas [15]. However, the lack of actual observations has made it impossible to effectively quantitatively assess the effectiveness of the correction, which remains a challenge.

In recent years, the rapid advancement of Artificial Intelligence (AI) has provided new opportunities for the development of radar and lidar signal processing. AI techniques have been applied to data assimilation [16], temporal-spatial wind field forecasting [17], nowcasting [18,19], extrapolation radar echoes [20,21], wind energy resource exploration [22], and signal denoising [23,24]. In addition to the multilayer neural network based method [15], some newly developed AI models could also offer the possibility for blockage correction. Generative Adversarial Networks (GANs) are a class of deep learning models proposed by Ian Goodfellow et. al. in 2014 [25]. GANs contain two parts: the Generator and the Discriminator. These two networks compete with each other during training as a way to improve performance. As a result, GANs can generate very high-quality data. GANs have been used in a variety of scenarios, including generation of high-quality images, image inpainting and super-resolution [26]. Image inpainting is the process of reconstructing missing parts of an image so that observers are unable to tell that these regions have undergone restoration. This technique is often used to remove unwanted objects from an image or to restore damaged portions of old photos. There are similarities between these scenarios and the reconstructions for beam blockages.

A GANs based method in conjunction with CDWL data is applied to solve the issue of beam blockages caused by low-altitude obstacles. This paper is organized as follows. Section 2 introduces the data sources and dataset construction. Section 3 presents the LOSV-filling network (LFnet) architecture and evaluation indicators. Section 4 studies the sensitivity of the reconstruction effectiveness with different shielding conditions and performs a practical application in an airport. Finally, a conclusion is drawn in Section 5.

2. Data

2.1. Data sources

The raw data is sourced from a CDWL, which is applied to detect horizontal windshear at a Guangzhou Baiyun International Airport (23°23'N, 113°17'E). It is operated at a wavelength of 1.5 μm . The lidar supports multiple scanning modes, and the Plan Position Indicator (PPI) mode is mainly applied. The elevation angles of PPI scanning are set as 3°, 4°, and 5°, respectively. The scanning angle of the azimuth of each PPI is from 0° to 360°, with a step angle of 3°. The period of one scanning is 1 minute, with a spatial resolution of 30 m. It's noteworthy that at elevation angles of 4° and 5°, the PPI scanning encounters no obstructions. At the elevation angle of 3°, obstructions due to low-altitude buildings such as airport towers, terminals, and fences exist, resulting in a lack of runway wind field detection data. In the experiment, data over 6 months is accumulated for this study.

2.2. Data preprocessing

The LOSV is obtained from the average Doppler shift of the power spectrum, using the maximum likelihood method or Gaussian fitting method [27]. The sign of LOSV is defined as positive when the movement is toward the lidar, and vice versa. The accuracy of the LOSV is determined by the ratio between the echo signal and noise (SNR). To ensure data quality, an SNR filter is applied to exclude wind data with low SNR. Considering the model's high requirements for dataset quality and the inherent attenuation of lidar signals with distance, the data within a range of 5000

m is selected for constructing the datasets, including the training set, the test dataset, and the validation dataset. The LOSV of these datasets should be complete, without any beam blockage. Thus, the PPI scanning suffered by beam blockage is removed. The radial spatial resolution of raw data is 30 m, while the angular resolution is 3°. The tangential spatial resolution increases with distance, thus the image of LOSV at a certain resolution is output by interpolation. The resolution of 256 × 256 pixels is chosen by considering computational complexity and model size. A total of 6940 PPI scanning with elevation angles of 4° and 5° is reserved. 70% of the dataset is used to form the training dataset, 20% for the test dataset, and 10% for the validation dataset.

Due to the impact of obstacles on the atmospheric dynamics, the airwake as a turbulent airflow will form around obstacles. When the obstacle is located at the upstream wind of the lidar, the core area affected by the airwake is not within the reconstruction area, which does not affect the reconstruction of the shielding area. However, when the obstacle is located the downstream of the lidar and the wind direction is nearly parallel to the emitting laser as well, it is difficult for the lidar to directly detect the core area of the airwake, resulting in the lack of training data for the airwake. In this situation, the reconstruction quality for the core affected area of the airwake is worse than that of the area far away from the airwake. Fortunately, this special situation is not common, and the core area affected by the airwake is only a few range gates with a resolution of 30 m. As for situations with large shielding angles, the reconstruction effect is poor due to the limited available edge information, even with a completed training set. Therefore, the impact of obstacle airwake is not considered when building the training set.

3. Methods

3.1. Model network architecture design

The LFnets architecture is presented in Fig. 1. The adversarial model [25,28] of GAN is used in this work. The generator is optimized with guidance from the discriminator, in the adversarial learning process. The aim of optimizing GAN is to attain a Nash equilibrium between the generator and discriminator. The process of optimizing GAN is similar to a min-max game between the generator and discriminator. The process is given as:

$$\min_G \max_D V(D, G) = \mathbb{E}_{x \sim p_{data}(x)} [\log D(x)] + \mathbb{E}_{z \sim p_z(z)} [\log(1 - D(G(z)))] \quad (1)$$

where \mathbb{E} represents the expectation about the distribution specified in the subscripts. D and G respectively represent the discriminator and generator, x denotes the sample and Z symbolizes the latent random vector of the generator. $p_{data}(x)$ and $p_z(z)$ represent input original data distribution and noise distribution. **Generator1** (G_1) and **Discriminator1** (D_1) are designed for the edge map generation, and **Generator2** (G_2) and **Discriminator2** (D_2) are designed for the reconstructed LOSV generation. The procedures of the LFnets are described as follows.

Step1, **input grayscale** image and **input mask map** for G_1 are prepared. The **input grayscale** image is grey-processed from the initial **unreconstructed LOSV** wind image. The **mask map** represents the shielding areas corresponding to the **grayscale** image. The **mask map** specifies the area that needs to be reconstructed. Various blockage scenarios are covered by these masks with adjusting shielding angles and ratios. In total, 360 masks were obtained for the training process.

Step2, **output edge map**, which captures the details of structural features of the LOSV, is obtained by G_1 and D_1 . The adversarial process begins with a grayscale image with dimensions of $H \times W$ (Height \times Width, 256 \times 256 pixels) along with a corresponding mask map. The data undergoes a sequence of dilated convolutional layers and residual blocks, which includes a pair of down-sampling encoders, eight **residual blocks**, and up-sampling decoders, resulting reconstructed feature-enhanced image with their original size. The feature-enhanced image is the **edge map** sent to D_1 . D_1 assumes responsibility for determining the real or fake of the **edge map** produced by G_1 and conversely guiding G_1 to improve the quality of the **edge map** through

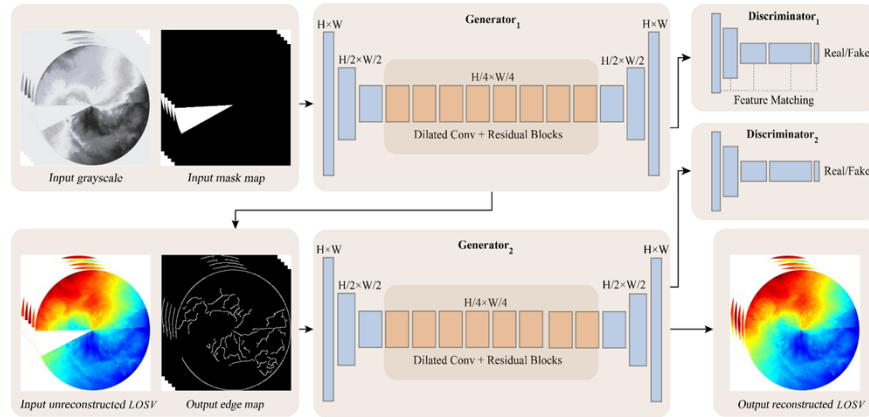


Fig. 1. The framework of the LFnet. G_1 captures the structural features of the grayscale and outputs the edge map of the masked area. G_2 adjusts the structural features of the unreconstructed LOSV by edge maps and outputs reconstructed LOSV.

feature matching. The feature matching loss L_{FM} is defined as

$$L_{FM} = \mathbb{E} \left[\sum_{i=1}^L \frac{1}{N_i} \|D_1^{(i)}(C_{gt}) - D_1^{(i)}(C_{pred})\|_1 \right] \quad (2)$$

where \mathbb{E} represents the expectation about the distribution specified in the subscripts. L represents the final convolution layer of the discriminator, and N_i represents the number of elements in the activation layer. D_1 utilizes a 70×70 pixels patch GAN architecture to identify the authenticity of overlapping image patches of 70×70 in size.

Step3, **the output reconstructed LOSV** is obtained by G_2 and D_2 . The **unreconstructed LOSV** and **edge map** is sent to G_2 . G_2 bears resemblance to G_1 structure as its main objective is to refine the structural features of the **unconstructed LOSV** to enhance the precision of the wind field data. The final output of this process is a 256×256 pixels **reconstructed LOSV** image that has been optimized to better reflect the observed data.

The LFnet is developed in the PyTorch framework. The training process started with the use of LOSV images as training data with a batch sample size of 8 to improve the efficiency of the process. The Adam optimizer [29] as one of the mainstream optimizers is employed as the training algorithm, allowing the learning rate to be automatically adjusted, thus enhancing the performance of the model. To stabilize the GAN training, spectral normalization (SN) [30], a weight normalization technique, is applied to the generator and discriminator [31]. Spectral normalization is chosen to save training time [28]. During the using of the Adam optimizer, the momentum term is stopped and only the RMSprop term is used. This means that it will behave exactly like the RMSprop optimizer. The learning rate of the discriminator is one-tenth of the learning rate of the generator. The initial learning rate of generators G_1 and G_2 is set to 10^{-4} , to fast convergence. When the loss values reached a plateau value, the learning rate is reduced to 10^{-5} , and the training persisted until a new convergence is achieved. In the final tuning phase, discriminator D_1 is removed, and both G_1 and G_2 are further trained at a reduced learning rate of 10^{-6} until the final convergence is confirmed.

3.2. Image quality evaluation indicators

Evaluating image quality has always been a critical issue in computer vision. Various indicators have been proposed, such as Peak Signal-to-Noise Ratio (PSNR), Structural Similarity Index

(SSIM) and Learned Perceptual Image Patch Similarity (LPIPS). PSNR was originally introduced by Shannon [32]. It is widely used to evaluate the quality of image or video compression. The calculation of PSNR involves taking the logarithm of the ratio of the peak signal to the mean squared error between the input signal and the compressed output signal. The PSNR is given by,

$$PSNR = 10 \log_{10} \left(\frac{a_{MAX}^2}{MSE} \right) \quad (3)$$

where MSE represent the mean-square error between the original and compressed signals, and a_{MAX} represent the maximum possible signal. However, PSNR can only quantify the average value of distortion, not considering localized cases of distortion.

The SSIM incorporates factors such as luminance, contrast and structure, aiming to compare the structural similarity between two images [33]. The SSIM is given by,

$$SSIM(x, y) = \frac{(2\mu_x\mu_y + c_1)(2\sigma_{xy} + c_2)}{(\mu_x^2 + \mu_y^2 + c_1)(\sigma_x^2 + \sigma_y^2 + c_2)} \quad (4)$$

where μ_x, μ_y are the average pixel values and $\sigma_x, \sigma_y, \sigma_{xy}$ are the variances and covariance of the images, respectively.

Furthermore, to evaluate the performance of GANs in image generation, the LPIPS is introduced by Richard Zhang [34]. LPIPS is a metric used to measure the perceptual similarity between two images. Unlike traditional PSNR and SSIM, LPIPS is learned through deep learning methods to better simulate human visual perception. The formula of LPIPS is not a simple mathematical formula but is implemented through deep neural networks. Typically, the LPIPS model uses two images as inputs and then outputs a perceptual similarity score between them. The specific architecture and parameters of the LPIPS model are obtained through large-scale training to capture the perceptual information of the images. The computation of LPIPS in this paper is done based on Python's lpips library. The LPIPS is given by,

$$d(x, x_0) = \sum_l \frac{1}{H_l W_l} \sum_{h,w} \|\omega_l \odot (\hat{y}_{hw}^l - \hat{y}_{0hw}^l)\|_2^2 \quad (5)$$

To obtain the d between reference and distorted patches x, x_0 with network \mathcal{F} , feature stack is extracted from L layers and unit-normalize in the channel dimension, which are designated as $\hat{y}^l, \hat{y}_0^l \in \mathbb{R}^{H_l \times W_l \times C_l}$ for layer l . The activations channel-wise is scaled by vector $w^l \in \mathbb{R}^{C_l}$ and computed with the ℓ_2 distance.

These traditional indicators are effective for conventional image processing applications, but they are not sufficient for evaluating the specific values of reconstructed lidar products. To solve this problem, a method for quantitative evaluation of reconstruction results is proposed, as shown in Fig. 2.

The reconstructed output is in the form of an image, which is characterized by the three numerical values of tricolor (RGB) ranging from 0 to 255. The color bar is divided into 256 parts, and each part corresponds to a specific LOSV value. Therefore, the output LOSV value of each grid point can be obtained by matching with the RGB of the color bar. The RGB difference between grid points and color bar (d_{ij}) can be calculated as,

$$d_{i,j,k} = \sqrt{(R_k - r_{i,j})^2 + (G_k - g_{i,j})^2 + (B_k - b_{i,j})^2} \quad (6)$$

where $(r_{i,j}, g_{i,j}, b_{i,j})$ and (R_k, G_k, B_k) represent the (i, j) grid point of the reconstructed area and the k_{th} color of the color bar, respectively. For each grid point, the index of k is determined, when the $d_{i,j,k}$ reaches its minimum value. The index k is then matched with a color bar to get the specific LOSV value of the grid point (i, j) .

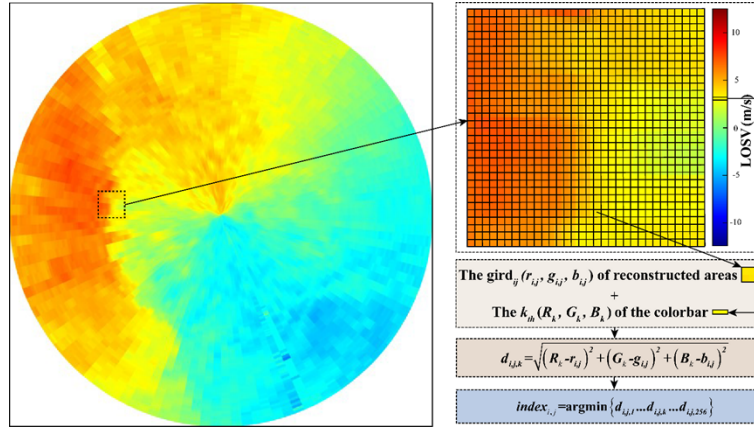


Fig. 2. The algorithm diagram for the inversion of specific LOSV values from the output image. The argmin is a function that retrieves the minimum value and returns the index.

The corresponding relationship between specific speed values and RGB of the output image is established. Based on this, in addition to perceptual indicators of PSNR, SSIM and LPIPS, prediction-specific indicators of Mean Absolute Error (MAE) and Root Mean Square Error (RMSE) are considered to evaluate the accuracy of output LOSV. MAE is given by:

$$MAE = \frac{1}{n} \sum_{i=1}^n |y_i^{LFnet} - y_i^{Real}| \quad (7)$$

where y_i^{Real} and y_i^{LFnet} represent the RGB value of LOSV without beam blockage and the RGB value of reconstructed LOSV, n is the number of grid points. RMSE is given by:

$$RMSE = \sqrt{\frac{1}{n} \sum_{i=1}^n (v_i^{LFnet} - v_i^{Real})^2} \quad (8)$$

where v_i^{Real} and v_i^{LFnet} represent the LOSV without beam blockage and the reconstructed LOSV, n is the number of grid points.

4. Result

4.1. Sensitivity analysis

This section focuses on assessing the effectiveness of the LFnet. The obstruction degree of the lidar signal by low-altitude obstacles depends on the radial and tangential obstruction ranges. The reconstruction effectiveness of different shielding angles and shielding ratios is assessed and analyzed. The test dataset is used instead of the training dataset. It consists of 1476 LOSV sets. Each wind set contains various blockage scenarios of mask maps with different shielding angles and shielding ratios. The shielding angle usually quantifies the degree of blockage in the tangential direction, which refers to the azimuth range of the blockage due to the low-altitude obstacles. In general, the obstruction has a greater impact on detection with a larger shielding angle. The shielding ratio is defined as the ratio of obstructed distance to the total distance in the radial direction. The higher the shielding ratio, the closer the obstruct is to the lidar, with the higher the degree of shielding.

To estimate the influence of the shielding angle on the LFnet's reconstruction performance, blockage reconstruction experiments were conducted at several shielding angles, including 5°,

15°, 20°, 30°, 35°, 40° and 50°, with a constant shielding ratio 100%. Output reconstruction results from different shielding angles are presented in Fig. 3.

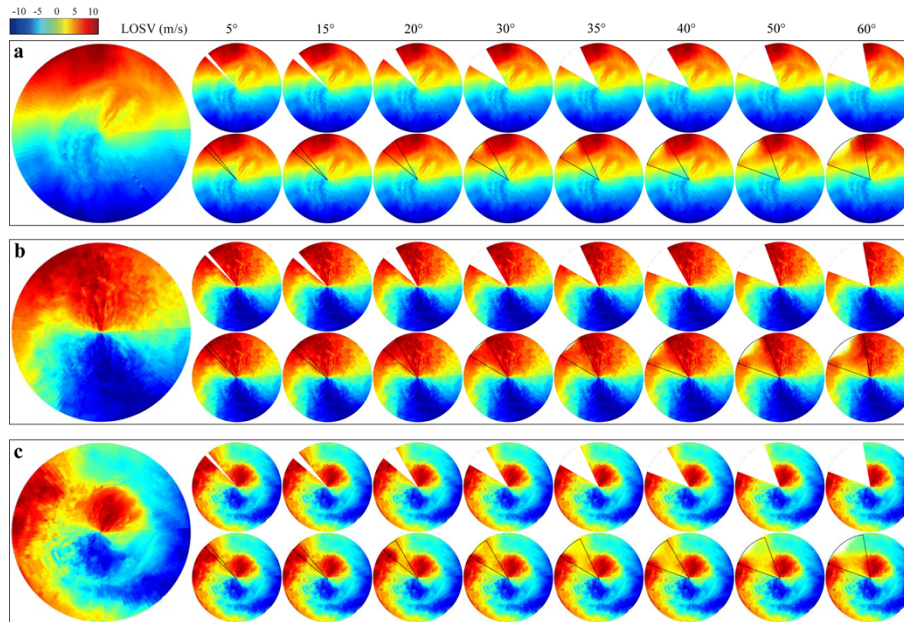


Fig. 3. Reconstruction effect of beam blockage under different shielding angles. The black dashed area is reconstructed. For each set, the bigger pictures on the left showcase the LOSV without beam blockage, and the first and second rows display the artificially blocked LOSV and the reconstructed LOSV.

Three typical LOSV sets are showcased. Figure 3(a) shows the uniform wind field. Figure 3(b) shows the wind field with windshear in the radial direction. Figure 3(c) shows the wind field with a gust front in the west. For each set, the bigger image on the left showcases the LOSV without beam blockage. The first and second rows display the artificially blocked LOSV and the reconstructed LOSV, respectively. The reconstructed LOSV matches well with the LOSV without beam blockage in small shielding angles. However, as the shielding angle increases, the reconstruction results in the far field will deteriorate, and the reconstructed area's integrity declines, with some structural features of the LOSV partially lost, as depicted in Fig. 3.

For evaluation of the beam blockage reconstruction experiments based on the LFnet, a range of indicators including PSNR, SSIM, LPIPS, MAE and RMSE are listed in Table 1. The standard deviations (SD) and the relative changes (RC) of these indicators are used to better compare different indicators and provide insight into the variability of reconstruction performance. The results of indicators are calculated based on the 1476 LOSV sets.

Among these, LPIPS, PSNR and SSIM are perceptual indicators, that simulate the human eye's intuitive perception to evaluate image quality. MAE and RMSE are predictive indicators, measuring absolute error. As the shielding angle increases, the reconstruction effect deteriorates and the RCs also increases. The RC of LPIPS, MAE and RMSE are much larger than those of PSNR and SSIM. As the shielding angle increases, the standard deviation of PSNR and SSIM does not change significantly, while the standard deviation of LPIPS and MAE increases and the reconstruction performance deteriorates. This trend indicates that perceptual differences become larger, implying a greater degree of distortion between the reconstructed LOSV and the LOSV without beam blockage. The values of MAE, RMSE and LPIPS increase with a larger shielding angle. A larger LPIPS value corresponds to weaker similarity between the LOSV without beam

Table 1. The indicators of different shielding angles.

Indicator		5°	10°	20°	30°	40°	50°
PSNR	Mean	41.528	35.069	28.6395	21.3065	18.8303	18
	SD	1.5269	1.354	1.9702	2.5883	2.55	2.4674
	RC	0.00%	-15.55%	-31.04%	-48.69%	-54.66%	-56.66%
SSIM	Mean	0.9991	0.9963	0.9865	0.9348	0.9031	0.8856
	SD	0.0244	0.0239	0.0234	0.0231	0.0229	0.0232
	RC	0.00%	-0.28%	-1.26%	-6.44%	-9.61%	-11.36%
LPIPS	Mean	0.006	0.007	0.0098	0.0154	0.0226	0.0316
	SD	0.0017	0.0021	0.0033	0.0067	0.0094	0.0112
	RC	0.00%	16.67%	63.33%	156.67%	276.67%	426.67%
MAE	Mean	0.0015	0.0027	0.0054	0.0131	0.0194	0.0229
	SD	0.0003	0.0004	0.0009	0.0021	0.0034	0.0042
	RC	0.00%	80.00%	260.00%	773.33%	1193.33%	1426.67%
RMSE	Mean	0.5118	0.7333	0.9736	1.3335	1.7192	2.0614
	RC	0.00%	43.28%	90.23%	160.55%	235.91%	302.77%

blockage and the reconstructed LOSV. The MAE and RMSE directly evaluate the specific error values of the real LOSV and the reconstruction LOSV. All of these indicators prove that as the shielding angle increases, the reconstruction effect will deteriorate.

Figure 4 shows the scatter density distribution and histograms of the reconstructed LOSV compared to the LOSV without beam blockage, covering a series of shielding angles with 100% of the shielding ratio. The RMSE and corresponding shielding angle are marked in each subplot. The RMSE increases from 0.51 m/s to 2.06 m/s, as the shielding angle increases from 5° to 50°. As shown in Fig. 4, with the shielding angle increasing, the reconstruction RMSE increases and the histogram of the LOSV difference widens, which means reconstruction performance deteriorates. Figure 4 also indicates that the error distribution is relatively uniform within the LOSV range of -9 m/s to 9 m/s. It can be inferred that the error of the reconstruction result is independent of the specific numerical value of LOSV.

In practical detection, beam blocking may occur at any position in the direction of laser propagation. To further study the influence of the shielding ratio on LFnet's reconstruction performance, blockage reconstruction experiments were conducted at several shielding ratios, including 10%, 20%, 30%, 40%, 50%, 60%, 70%, 80%, with a constant shielding angle of 25°. Output reconstruction results from different shielding ratios are presented in Fig. 5. Three typical LOSV sets, similar to Fig. 3 are presented. Overall, the reconstructed LOSV matches well with the LOSV without beam blockage in small shielding ratios.

In Fig. 5, the dashed line annular sector area represents the reconstruction result. As the shielding ratio increases, the black annular sector area to be reconstructed increases, while the available structural features information in the radial direction decreases. The reduction of available structural features will increase the reconstruction error in the far field, especially in the edge region. For example, when the shielding ratio is 10%, the velocity structure feature at the edge is successfully reconstructed. However, when the shielding ratio reaches 80%, the reconstructed LOSV at the edge tend to be inconsistent.

To evaluate the overall reconstruction effect, the evaluation indicators are listed in Table 2. Consistent with the sensitivity experiment of shielding angles, the results of indicators are calculated based on the 1476 LOSV sets. As the shielding ratio increases, the reconstruction effect deteriorates and the RCs also increases. These results also support that the larger the shielding ratio, the worse the overall reconstruction effect. A high shielding ratio corresponds to

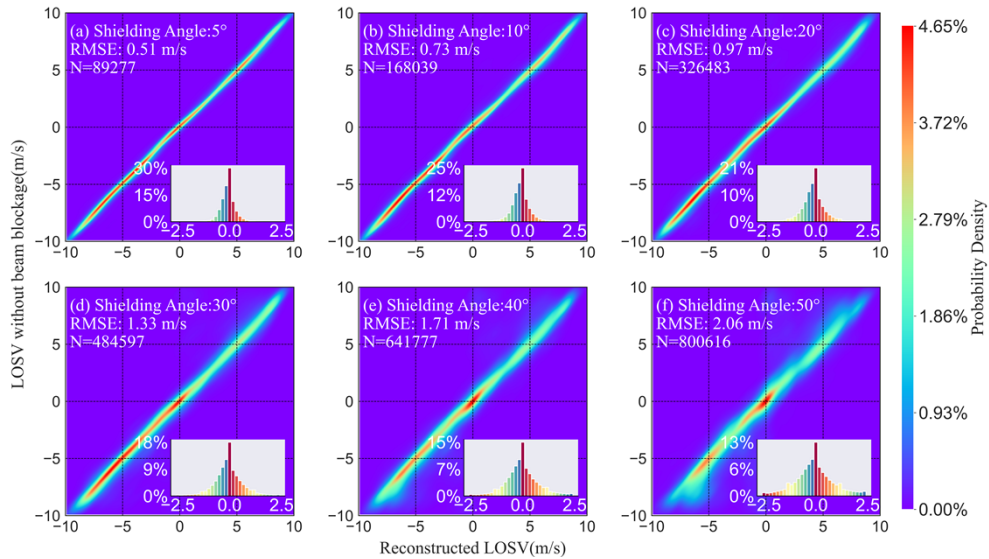


Fig. 4. Scatter plots and differences histograms between the LOSV without beam blockage and reconstructed LOSV with the differing shielding angle.

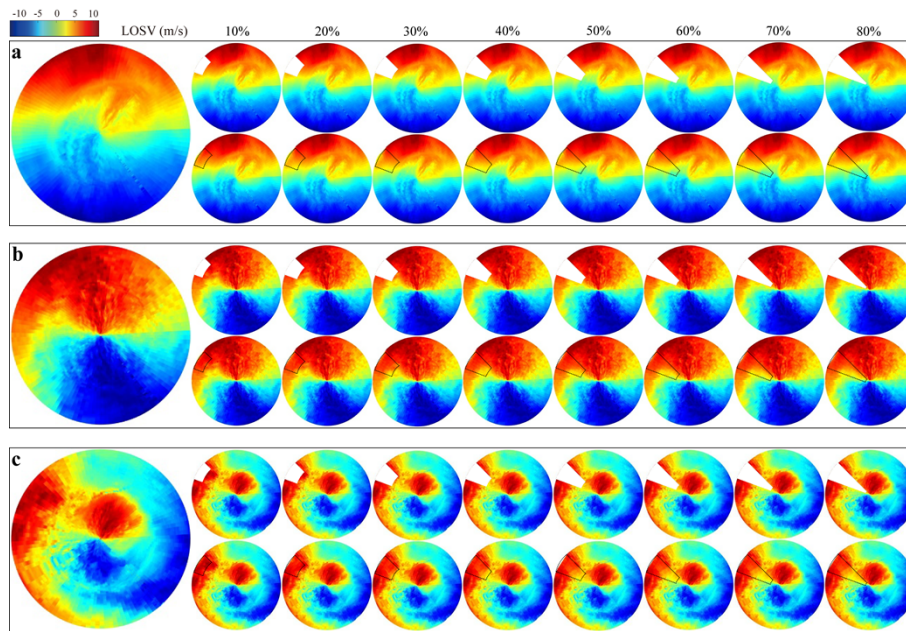


Fig. 5. Reconstruction effect of beam blockage under different shielding ratios. The black dashed area is reconstructed. One of the bigger pictures on the left showcases the LOSV without beam blockage. The first and second rows in (a)-(c) display the artificially blocked LOSV and the reconstructed LOSV.

a larger area to be reconstructed with less available structural feature information, resulting in high difficulty in reconstruction and an increase in the reconstruction error. Specifically, RMSE increases from 1.18 m/s to 1.72 m/s, as the shielding ratio increases. In Table 1 and Table 2, as the shielding angle increases or shielding ratio increases, SD of indicators also increases, indicating the deterioration of reconstruction. However, SD of indicators in Table 1 changes more significantly, compared with SD of indicators in Table 2. It means that the reconstruction performance is more sensitive to the shielding angle than shielding ratio. In summary, the reconstruction result in the low shielding ratio is better than that in the high shielding ratio.

Table 2. The indicators of different shielding ratios under 25° shielding angle.

Indicator		10%	20%	30%	40%	50%	60%	70%	80%
PSNR	Mean	32.5475	30.1413	29.8507	29.7087	29.5332	29.3709	29.2986	29.2408
	SD	2.4673	2.4811	2.4829	2.5227	2.497	2.5394	2.6323	2.4932
	RC	0.00%	-7.39%	-8.29%	-8.72%	-9.26%	-9.76%	-9.98%	-10.16%
SSIM	Mean	0.9957	0.9928	0.9914	0.9912	0.9902	0.9892	0.989	0.9888
	SD	0.0231	0.0231	0.0232	0.0231	0.0231	0.0236	0.0239	0.024
	RC	0.00%	-0.29%	-0.43%	-0.45%	-0.55%	-0.65%	-0.67%	-0.69%
LPIPS	Mean	0.0121	0.0119	0.0117	0.0113	0.011	0.0105	0.01	0.0094
	SD	0.005	0.005	0.0049	0.0049	0.0046	0.0043	0.0041	0.0037
	RC	0.00%	-1.65%	-3.31%	-6.61%	-9.09%	-13.22%	-17.36%	-22.31%
MAE	Mean	0.0035	0.0045	0.005	0.0051	0.0054	0.0056	0.0057	0.0058
	SD	0.0009	0.0009	0.0009	0.0009	0.0008	0.0009	0.0009	0.0009
	RC	0.00%	28.57%	42.86%	45.71%	54.29%	60.00%	62.86%	65.71%
RMSE	Mean	1.1828	1.1942	1.219	1.2578	1.3187	1.3986	1.5443	1.7205
	RC	0.00%	0.96%	3.06%	6.34%	11.49%	18.24%	30.56%	45.46%

Figure 6 shows the scatter density plot of the reconstructed LOSV compared to the LOSV without beam blockage, covering various shielding ratios with the shielding angle remaining fixed at 25°. The change in the histogram of the LOSV difference is not obvious, indicating that the reconstruction error is not sensitive to the shielding ratio. It is consistent with the change of RMSE. The LOSV without beam blockage and the reconstructed LOSV have good consistency and have limited variation with the shielding ratio. Under a small shielding angle condition, the contribution of shielding ratios to the accuracy of the reconstruction output is smaller, compared to the contribution of shielding angles to the RMSE.

The reconstruction of shielding areas mainly utilizes the available structural features information of adjacent areas. No matter what shape of small area of shielding area, in most cases there is enough available structural features information, resulting in a good reconstruction performance. With the same large area, narrow shaped areas have more available structural features information than that of flat areas, with a better reconstruction performance. Therefore, the reconstruction effect depends on the shape of the area, which is determined by the shielding angle and shielding ratio. To comprehensively investigate the impact of these two shielding conditions on reconstruction performance, the sensitivity of the LFnet performance under different shielding conditions is further explored. The shielding angle is from 5° to 60°, with a step of 5°. The shielding ratio is from 10% to 90%, with a step of 10%. In a total of 108 different shielding conditions are applied. The experimental data consists of 1476 LOSV with several mask datasets. The RMSE under different shielding conditions is used to assess the quality of output results, as shown in Fig. 7(a). Although an increase in both shielding angles and ratios can lead to an increase in RMSE, the shielding angle is the dominant factor in the reconstruction error, when the shielding angle is less than 25°. In the case of small shading angles, the correlation

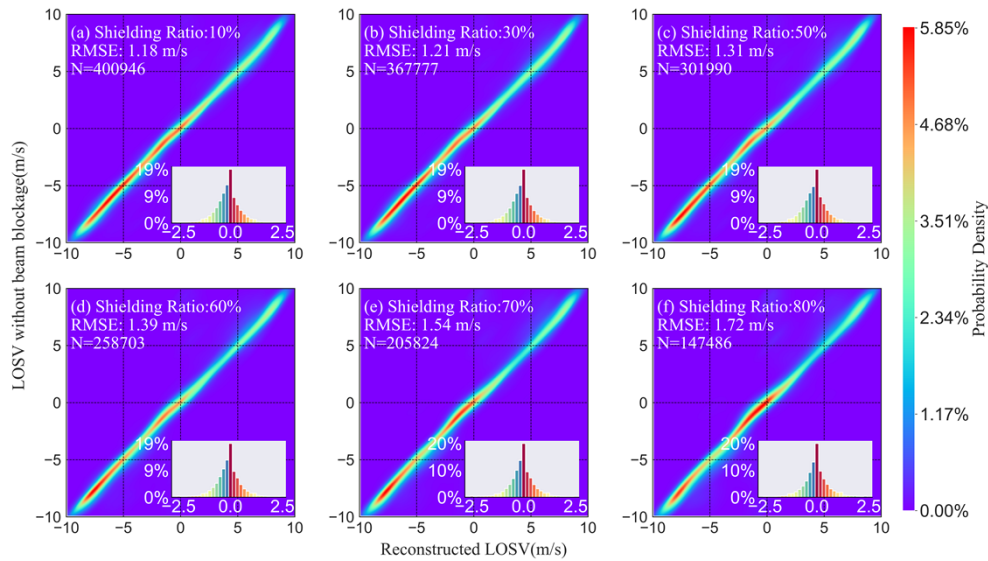


Fig. 6. Scatter plots and differences histograms between the LOSV without beam blockage and reconstructed LOSV with the differing shielding ratio.

between the velocity structure features in the tangential direction on both sides is high, resulting in less difficult reconstruction and insensitive to shielding ratios. The RMSE is less than 1 m/s in different shielding ratios when the shielding angle is less than 25° . As the shielding angle increases from 25° , the contribution of the shielding ratio to the reconstruction error begins to increase. When the shielding angle is greater than 45° , the shielding ratio is the main contribution to the reconstruction error. A large shielding angle corresponds to a large arc length, which leads to less available structural feature information, causing deterioration of reconstruction results.

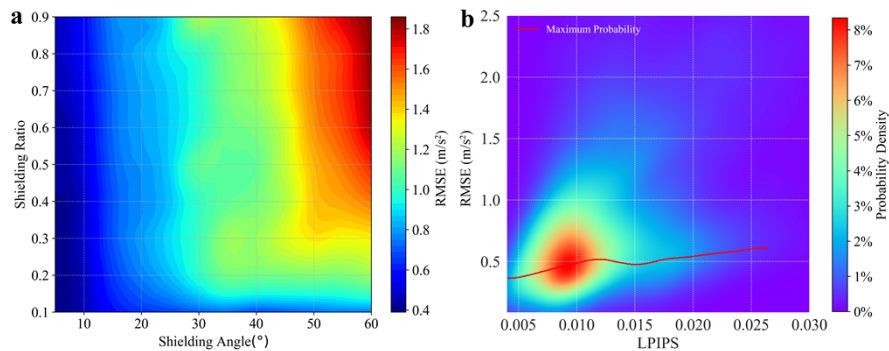


Fig. 7. (a) RMSE under different shielding conditions. (b) Kernel density distribution of LPIPS and RMSE. The blue dotted line is the fitting function between RMSE and LPIPS fitting. The red solid line is the maximum probability density line.

Figure 7(b) depicts the kernel density distribution of LPIPS and RMSE under various shielding conditions. The red solid line illustrates the line of maximum probability density. The LPIPS captures the similarity between reconstructed and real LOSV, serving as a measurement of their resemblance. The LPIPS and RMSE have a clear correlation when the LPIPS is less than 0.012. As the LPIPS increases from 0.012, it shows a weak relationship between the LPIPS and RMSE. In practical applications with obstruction, evaluating the quality of reconstructed LOSV is a

challenge due to the absence of real LOSV in shielding areas. Therefore, conventional evaluation indicators such as LPIPS are solely applicable to the validation set and cannot be extended to evaluate the performance of obstruction reconstruction in practical applications. Compared with LPIPS, the RMSE evaluation method proposed in this paper offers a direct assessment of the LFnet reconstruction performance. For the specified shielding angle and shielding ratio, the reconstruction overall error can be estimated by query with Fig. 7(a).

4.2. Application example

In the field experiment of the airport, the PPI scanning results with an elevation of 3° have several obstructions due to airport towers, terminals, and fences. To reconstruct the lacking wind field on the runway, the LFnet is applied to reconstruct the shielding area, as shown in Fig. 8. The actual detected LOSV after quality control and the corresponding mask of the shielding area are shown in Fig. 8(a) and Fig. 8(b). The actual detected LOSV and the mask are input into the LFnet, which outputs the reconstructed LOSV as shown in Fig. 8(c). There typical wind fields are demonstrated with the LFnet, including wind fields with characteristics of windshear, turbulence, and gust front. The first row shows the reconstruction results of a wind shear event. At a distance of 2 km to the north of the lidar, the LOSV has increased from 2.5 m/s to over 7 m/s. The second row reconstructs the non-uniform motion characteristics of turbulence. The third row represents a gust front process existing in west. Overall, the reconstruction results successfully capture the speed structure in various wind farms.

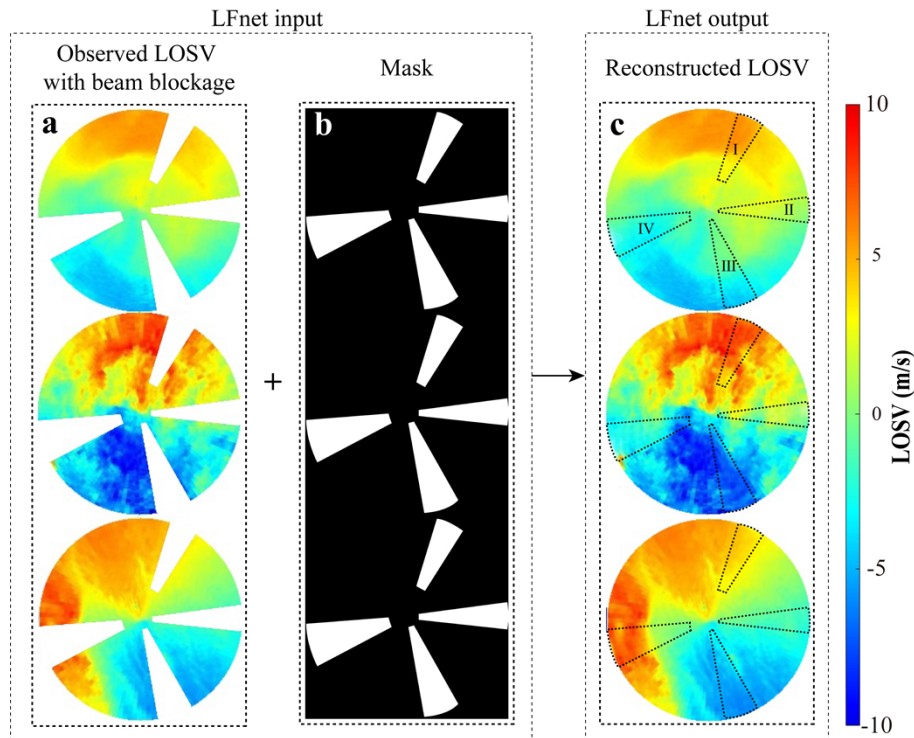


Fig. 8. Reconstruction process. (a) Actual detected LOSV with beam blockage. (b) Corresponding mask. (c) Reconstructed LOSV. The four shielding areas are I, II, III, and IV.

The specific reconstruction performance is assessed with the proposed RMSE method, as shown in Table 3. There were four shielding areas, with shielding angles of 13.6° , 16.3° , 18.8°

and 21.4° , corresponding to the shielding ratio of 69.1%, 85.1%, 87.5%, and 78.9%, respectively, which are marked as I, II, III, and IV. Based on the shielding angle and shielding ratio, the RMSE of the four reconstruction areas can be estimated based on Fig. 7(a), which are 0.68 m/s, 0.78 m/s, 0.80 m/s and 0.85 m/s, respectively. It can infer that the RMSE between the real LOSV and the reconstructed LOSV does not exceed 0.85 m/s.

Table 3. The RMSE of the four reconstruction areas

Shielding area	Shielding angle	Shielding ratio	RMSE
I	13.6°	69.1%	0.68 m/s
II	16.3°	85.1%	0.78 m/s
III	18.8°	87.5%	0.80 m/s
IV	21.4°	78.9%	0.85 m/s

Figure 9 shows the continuous process of an easterly gust front, from 15:02 to 17:52 on December 27, 2022. The observed LOSV with the elevation angle of 3° are existing beam blockages, as shown in Fig. 9(a). The corresponding reconstruction LOSV output by LFnet is shown in Fig. 9(b). As the lidar elevation angle rises to 4° , the detected LOSV is complete without beam blockage, which is set as the control LOSV set, as shown in Fig. 9(c). The reconstruction LOSV well captured the process of a gust front. The captured features are very similar to the control group, which verifies the effectiveness of the reconstruction results to some extent.

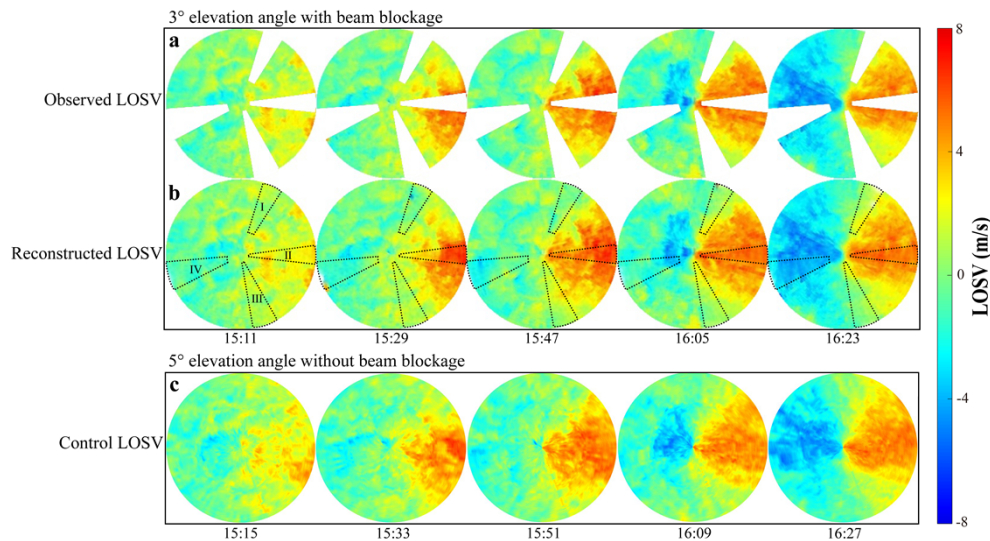


Fig. 9. Example of the evolution of a continuous wind field with an elevation angle of 3° . (a) Observed LOSV with an elevation angle of 3° . (b) Reconstructed LOSV with an elevation angle of 3° . (c) Control LOSV without beam blockage with an elevation angle of 4° . The dashed box represents the reconstruction area.

At 15:11, the wind field was stable with some turbulence, and an easterly gust front began to appear in the east. At 15:47, the gust front arrived above the lidar and towered over the west, with a maximum wind speed of 8 m/s. At 16:23, the gust front had already passed westward through the lidar, affecting the entire airport glide path. Under the influence of the gust front, it is easy to cause windshear and lead to aircraft queuing. The angle between the glide path and the ground is about 3° in the landing process of a flight. Therefore, the reconstruction of the wind field at this elevation angle plays an indispensable role in ensuring the landing of the flight.

5. Conclusion

This paper proposes the LFnet method aiming to solve the issues of beam blockage reconstruction and its quantitatively evaluation for CDWL detection. Firstly, the LOSV dataset for the LFnet is derived from field experiments conducted at an airport, with masks created to simulate shielding phenomena for the training of the LFnet. Subsequently, in the test set, the sensitivity of the reconstruction effectiveness with different shielding conditions is systematically analyzed. Results show that the available structural features information determines the reconstruction quality of the LFnet, and the amount of structural features information is determined by the shielding conditions. The increase in shielding angle and shielding ratio will lead to an increase in reconstruction error. The shielding angle affects the available tangential structural features, while the shielding ratio affects the radial feature information. At small shielding angles, tangential information is sufficient resulting in a good reconstruction performance. Whereas at large shielding angles, whose reconstruction relies on radial information, the shielding ratio is the dominant factor.

One of the main challenges in the field of image reconstruction is evaluating the quality of the reconstruction, as traditional evaluation indicators like the LPIPS is limited to the validation set. However, the proposed RMSE evaluation method offers a direct assessment of the LFnet reconstruction performance. The reconstruction error can be estimated by query with the relationship between RMSE and shielding condition without real value. In practical application, this work has successfully reconstructed the complete process of an easterly gust front in the airport, which provides a complete wind field for flight safety. This method is not only effective for the LOSV reconstruction in CDWL, in the future, we will extend the method to other products in lidar and radar, such as spectral width and echo intensity. Due to the limitations of the training set, the LFnet is not applicable for reconstructing shielding areas within the core affected area of the airwake. The impact of obstacle airwake is still an issue, which should be addressed. In the future, we will apply computational fluid dynamics (CFD) technology to simulate obstacle airwake and generate virtual lidar scanning data, to improve the reconstruction effect on obstacle airwake areas.

Funding. Chinese Aeronautical Establishment (202300220R2001); Natural Science Foundation of Jiangsu Province (BK20230434).

Disclosures. The authors declare no conflicts of interest.

Data availability. Data underlying the results presented in this paper are not publicly available at this time but may be obtained from the authors upon reasonable request.

References

1. Z. Liu, J. F. Barlow, P.-W. Chan, *et al.*, "A Review of Progress and Applications of Pulsed Doppler Wind LiDARs," *Remote Sens.* **11**(21), 2522 (2019).
2. L. Thobois, J. P. Cariou, and I. Gultepe, "Review of Lidar-Based Applications for Aviation Weather," *Pure Appl. Geophys.* **176**(5), 1959–1976 (2019).
3. P. W. Chan, "LIDAR-based turbulence intensity calculation using glide-path scans of the Doppler Light Detection And Ranging (LIDAR) systems at the Hong Kong International Airport and comparison with flight data and a turbulence alerting system," *Meteorol. Z.* **19**(6), 549–563 (2010).
4. V. A. Banakh and I. N. Smalikho, "Lidar Studies of Wind Turbulence in the Stable Atmospheric Boundary Layer," *Remote Sens.* **10**(8), 1219 (2018).
5. F. Pantillon, A. Wieser, B. Adler, *et al.*, "Overview and first results of the Wind and Storms Experiment (WASTEX): a field campaign to observe the formation of gusts using a Doppler lidar," in *Advances in Science and Research* (Copernicus GmbH, 2018), 15, pp. 91–97.
6. J. Yuan, L. Su, H. Xia, *et al.*, "Microburst, Windshear, Gust Front, and Vortex Detection in Mega Airport Using a Single Coherent Doppler Wind Lidar," *Remote Sens.* **14**(7), 1626 (2022).
7. T.-C. Wu and K. Hon, "Application of spectral decomposition of LIDAR-based headwind profiles in windshear detection at the Hong Kong International Airport," *Meteorol. Z.* **27**(1), 33–42 (2018).
8. H. Zhang, S. Wu, Q. Wang, *et al.*, "Airport low-level wind shear lidar observation at Beijing Capital International Airport," *Infrared Phys. Technol.* **96**, 113–122 (2019).
9. P. Nechaj, L. Gaál, J. Bartok, *et al.*, "Monitoring of Low-Level Wind Shear by Ground-based 3D Lidar for Increased Flight Safety, Protection of Human Lives and Health," *Int. J. Environ. Res. Public Health* **16**(22), 4584 (2019).

10. J. Yuan, H. Xia, T. Wei, *et al.*, "Identifying cloud, precipitation, windshear, and turbulence by deep analysis of the power spectrum of coherent Doppler wind lidar," *Opt. Express* **28**(25), 37406–37418 (2020).
11. I. N. Smalikho, V. A. Banakh, F. Holzäpfel, *et al.*, "Method of radial velocities for the estimation of aircraft wake vortex parameters from data measured by coherent Doppler lidar," *Opt. Express* **23**(19), A1194–A1207 (2015).
12. P. C. Shakti, M. Maki, S. Shimizu, *et al.*, "Correction of Reflectivity in the Presence of Partial Beam Blockage over a Mountainous Region Using X-Band Dual Polarization Radar," *J. Hydrometeorol.* **14**(3), 744–764 (2013).
13. P. Zhang, D. Zrnica, and A. Ryzhkov, "Partial Beam Blockage Correction Using Polarimetric Radar Measurements," *J. Atmospheric Ocean. Technol.* **30**(5), 861–872 (2013).
14. X. Huang, L. Ma, and M. Yang, "Recognition and correction of beam blockage of weather radar based on spatial correlation," *J. Meteorol. Sci.* **39**(4), 532–539 (2019).
15. X. Yin, Z. Hu, J. Zheng, *et al.*, "Study on Radar Echo-Filling in an Occlusion Area by a Deep Learning Algorithm," *Remote Sens.* **13**(9), 1779 (2021).
16. H. Gao, J. Zhou, P.-W. Chan, *et al.*, "A Hybrid Method for Fine-Scale Wind Field Retrieval Based on Machine Learning and Data Assimilation," *IEEE Trans. Geosci. Remote Sens.* **60**, 1 (2022).
17. J. Zhang and X. Zhao, "Spatiotemporal wind field prediction based on physics-informed deep learning and LIDAR measurements," *Appl. Energy* **288**, 116641 (2021).
18. S. Guo, N. Sun, Y. Pei, *et al.*, "3D-UNet-LSTM: A Deep Learning-Based Radar Echo Extrapolation Model for Convective Nowcasting," *Remote Sens.* **15**(6), 1529 (2023).
19. L. Han, Y. Zhao, H. Chen, *et al.*, "Advancing Radar Nowcasting Through Deep Transfer Learning," *IEEE Trans. Geosci. Remote Sens.* **60**, 1–9 (2022).
20. A. Gong, R. Li, B. Pan, *et al.*, "Enhancing Spatial Variability Representation of Radar Nowcasting with Generative Adversarial Networks," *Remote Sens.* **15**(13), 3306 (2023).
21. Y. Hu, L. Chen, Z. Wang, *et al.*, "Towards a More Realistic and Detailed Deep-Learning-Based Radar Echo Extrapolation Method," *Remote Sens.* **14**(1), 24 (2021).
22. S. Shamsirband, T. Rabczuk, and K.-W. Chau, "A Survey of Deep Learning Techniques: Application in Wind and Solar Energy Resources," *IEEE Access* **7**, 164650–164666 (2019).
23. O. Kliebisch, H. Uittenbosch, J. Thurn, *et al.*, "Coherent Doppler wind lidar with real-time wind processing and low signal-to-noise ratio reconstruction based on a convolutional neural network," *Opt. Express* **30**(4), 5540–5552 (2022).
24. Y. Song, Y. Han, Z. Su, *et al.*, "Denoising coherent Doppler lidar data based on a U-Net convolutional neural network," *Appl. Opt.* **63**(1), 275–282 (2024).
25. I. Goodfellow, J. Pouget-Abadie, M. Mirza, *et al.*, "Generative Adversarial Nets," in *Advances in Neural Information Processing Systems* (Curran Associates, Inc., 2014), 27.
26. H. Alqahtani, M. Kavakli-Thorne, and G. Kumar, "Applications of Generative Adversarial Networks (GANs): An Updated Review," *Arch. Comput. METHODS Eng.* **28**(2), 525–552 (2021).
27. J. Yuan, Y. Wu, Z. Shu, *et al.*, "Real-Time Synchronous 3-D Detection of Air Pollution and Wind Using a Solo Coherent Doppler Wind Lidar," *Remote Sens.* **14**(12), 2809 (2022).
28. K. Nazeri, E. Ng, T. Joseph, *et al.*, "EdgeConnect: Generative Image Inpainting with Adversarial Edge Learning," *arXiv*, arXiv:1901.00212 (2019).
29. D. P. Kingma and J. Ba, "Adam: A method for stochastic optimization," *arXiv*, arXiv:1412.6980 (2014).
30. T. Miyato, T. Kataoka, M. Koyama, *et al.*, "Spectral Normalization for Generative Adversarial Networks," *arXiv*, arXiv:1802.05957 (2018).
31. H. Zhang, I. Goodfellow, D. Metaxas, *et al.*, "Self-Attention Generative Adversarial Networks," in *Proceedings of the 36th International Conference on Machine Learning* (PMLR, 2019), pp. 7354–7363.
32. C. E. Shannon, "A mathematical theory of communication," *Bell Syst. Tech. J.* **27**(3), 379–423 (1948).
33. D. G. Lowe, "Distinctive Image Features from Scale-Invariant Keypoints," *Int. J. Comput. Vis.* **60**(2), 91–110 (2004).
34. R. Zhang, P. Isola, A. A. Efros, *et al.*, "The Unreasonable Effectiveness of Deep Features as a Perceptual Metric," in *Conference on Computer Vision and Pattern Recognition* (IEEE, 2018).